

Development of a New High-Resolution Angle-Sensing Mechanism Using an RGB Sensor

Young-shin Kwon, *Student Member, IEEE*, and Won-jong Kim, *Senior Member, IEEE*

Abstract—A new high-resolution angle-sensing mechanism using a color sensor is presented in this paper. This scheme is based on a red–green–blue (RGB) sensor that measures the radiant-intensity variation of the light reflected off a colored surface. The propagation mechanism for the output of an RGB sensor due to the reflected light's intensity on the cylindrical color track printed with the designated RGB codes from a light-emitting-diode source is discussed. The angle discrepancies due to color-printer characteristics and paper roughness are compensated for by a quarter-error compensation formula and the reference angles using a precision potentiometer. Through the performance verification of the new angle-sensing mechanism with a rotary position-control test bed in frequency and time domains, the feasibility of this new cost-effective noncontact angle-sensing mechanism is demonstrated. The bandwidth of 4.42 kHz, resolution of 0.08°, and nonlinearity of 6.63% are achieved.

Index Terms—Angle-sensing, light-emitting diode (LED), position control, red–green–blue (RGB) sensor.

I. INTRODUCTION

THE rotation angle in rotary position-control systems is a primary variable to control [1]. Hence, the angle sensor is required to be accurate, sensitive, and cost-effective. Many angle-measuring sensors based on various working principles were studied and produced in the last five decades. Currently, key angle sensors such as rotary potentiometers, optical encoders, and resolvers are used in many precision-motion-control systems in scientific, industrial, military, and medical applications. However, the linearity degradation of the potentiometer due to carbon debris or resistive-surface erosion remains an unsettled drawback in a long-term operation [2], [3]. The absolute encoder using a natural code may detect a faulty digital number for a brief moment with all the bits not changing simultaneously when the encoder crosses over from one section to the next [4]. The high cost of the resolver and resolver-to-digital converter is also an entry barrier in low-cost commercial applications despite its ruggedness and high precision [5]–[8].

In order to overcome these drawbacks, noncontact angular position sensors using ferromagnetic disks and CMOS Hall sensors were developed [9], [10]. A multisensor approach through the

spatial arrangement of Hall-effect sensors in order to achieve a nanodegree angular positional accuracy was introduced by Foong *et al.* [11]. Another low-cost angle sensor using a semi-ring magnet and linear Hall-effect sensors was presented with the accuracy of $\pm 0.6^\circ$ in the range of 0° – 360° [12]. Fulmek *et al.* [13] developed a low-cost, robust, and contactless capacitive angle-sensing system with a relative angular range of $\pm 7.5^\circ$ with a resolution of 0.1° . Cheng *et al.* [14] proposed a low-cost cylindrical capacitive sensor that can detect the whirling motion caused by the eccentric motion with the resolution of smaller than 1 pF. Kimura *et al.* [15] also developed a resolver-compatible capacitive rotary position sensor that can directly replace a commercial resolver with the maximum nonlinearity error of $\pm 4.0^\circ$. An optoelectronic joint-angle sensor for tendon-driven robot fingers was explored using a coupled light-emitting diode (LED)/photodiode instead of conventional rotary angle sensors [16]. Multiple-degree-of-freedom sensors based on the noncontact optical sensing mechanism that detects microscopic changes in consecutive images have been extensively researched [17]–[21]. However, in spite of these various attempts, most research activities for emerging RGB sensors focused on object sorting, color identification, target recognition, and color detection of the object's surface so far [22]–[25].

This paper presents a novel high-resolution angle-sensing mechanism using an RGB sensor. This sensing mechanism presents significant advantages, such as noncontact sensing, absolute angle measurement, and a cost-effective measuring circuit. For this purpose, a propagation model and an error-compensation technique for this new sensing mechanism are described in detail. A rotary position-control test bed is also developed to verify its performance. Finally, the feasibility of this proposed cost-effective noncontact rotary angle-sensing mechanism is demonstrated with remarkable experimental results.

II. ANGLE-SENSING MECHANISM

The RGB angle-sensing module consists of three parts—an LED light source, a cylindrical color track, and an RGB sensor. The schematic shown in Fig. 1 illustrates their geometrical configuration. The light emitted from an LED illuminates the cylindrical color track printed with the designated RGB codes corresponding to the specific angle. The RGB sensor measures the radiant intensity of the light reflected on the color track and generates a reverse-bias current in proportion to the radiant intensity of the reflected light. A built-in photodiode amplifier in the RGB sensor transforms the reverse-bias current to a significant voltage level to measure. The voltage signal is translated into an absolute angle by an angle-sensing constant. In this section, the step-by-step procedure to obtain the dynamic

Manuscript received May 1, 2013; revised September 4, 2013; accepted November 16, 2013. Date of publication December 18, 2013; date of current version May 16, 2014. Recommended by Technical Editor S. Fatikow.

The authors are with the Department of Mechanical Engineering, Texas A&M University, College Station, TX 77843-3123 USA (e-mail: y.s.kwon@tamu.edu; wjkim@tamu.edu).

Color versions of one or more of the figures in this paper are available online at <http://ieeexplore.ieee.org>.

Digital Object Identifier 10.1109/TMECH.2013.2293571

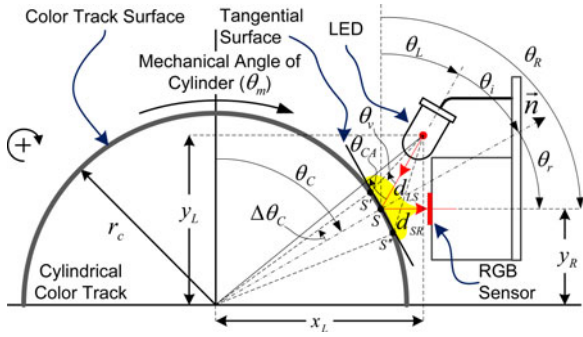


Fig. 1. Two-dimensional cross-sectional view of the angle-sensing mechanism (illumination and reflection configuration).

propagation model for the angle-sensing mechanism is presented in detail.

A. Geometrical Configuration for the Sensing System

The object's surface reflects the light in various ways as the specular surface, Lambertian surface, and specular diffusion according to its texture or the wavelength of light [26], [27]. In this paper, the roughness of the color-coated paper is assumed to be slightly less than the wavelength of the LED light, so a conventional directional diffusion model is used as the surface reflectance model [28], [29]. In such a case, since the main transmitting power still lies on the specular line as shown in Fig. 1, when the viewing angle (θ_v) of the LED is zero, the geometrical relation among the mechanical angle (θ_L) of the LED, the arc angle (θ_C) of the point S , and the mechanical angle (θ_R) of the RGB sensing face is given as (1) because the incident angle (θ_i) is equal to the reflection angle (θ_r)

$$\theta_R = \theta_L + 2\theta_i = \theta_L + 2(\theta_C - \theta_L) = 2\theta_C - \theta_L. \quad (1)$$

The incident angle due to the arbitrary viewing angle of the LED can also be written as

$$\theta_i = \theta_C - \theta_L - \theta_v + \Delta\theta_c \quad (2)$$

where $\Delta\theta_c = -d_{LS} \sin \theta_v / (r_C \cos(\theta_C - \theta_L - \theta_v))$, d_{LS} is the distance from the light origin of the LED to the point S , and r_C is the radius of the cylindrical track. The critical angle (θ_{CA}) for the full viewing angle is given by

$$\theta_{CA} = \tan^{-1} \left(\frac{r_C \sin \theta_C + d_{LS} \sin \theta_L}{r_C \cos \theta_C + d_{LS} \cos \theta_L} \right) - \theta_L. \quad (3)$$

Herein, in order to avoid the refraction effect due to the plastic cover of the RGB sensor and the interference due to the direct emitted light from the full viewing angle of the LED, θ_R , θ_L , and θ_C are determined as 90° , 30° , and 60° , respectively, so that the specular line lies in perpendicular to the sensing face.

B. Resolution and the Angle-Detection Principle

The RGB coded pattern using the red color (that is, green and blue have zero RGB values) depicted in Fig. 2 shows that the angular resolution of the RGB sensor is determined by the diameter of the beam and the rectangular cell printed with a designated RGB code per the interval of 1.0° . For example, if the

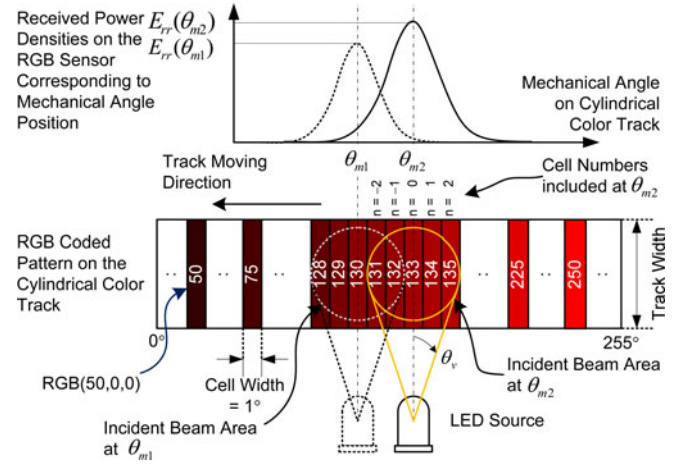


Fig. 2. Power densities due to the red RGB-coded track and the incident area illuminated by the LED.

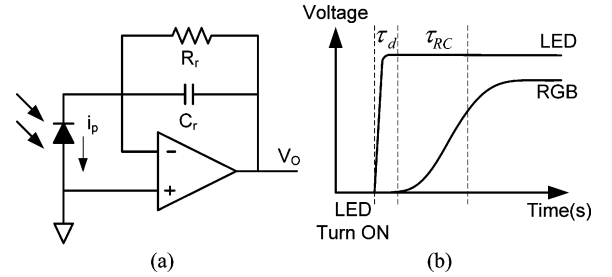


Fig. 3. (a) Current-to-voltage converter circuit of the RGB sensor and (b) time response between transmission and reception.

diameter of the incident-beam area is less than the rectangular cell width, the resolution will be 1.0° because the irradiance change can occur only when the incident cell changes. In contrast, if the diameter of the incident-beam area is bigger than the cell width, the analog output voltage of the RGB sensor becomes the sum of irradiance reflected from several red RGB-coded colors. This reveals that since the value of the sum can vary even with a tiny motion, the angle-sensing resolution becomes theoretically infinite. Thus, the actual resolution is limited by the resolution of the analog-to-digital converter (ADC) if there is no noise or nonlinearities. The normal distributions described in Fig. 2 show the varying power densities of the reflected light in accordance with the movement of the incident-beam area due to the rotation of the cylindrical color track. As a result, the output of the RGB sensor indicates the mechanical angular displacement.

C. Dynamic Model Between the LED and the RGB Sensor

Since the LED is used as a constant light source in this paper, the dynamic model between the LED source and the RGB sensor can be derived from the propagation delay time and the time constant of the current-to-voltage converter built in the RGB sensor as shown in Fig. 3.

From Fig. 1, the propagation delay (τ_d) can be calculated by

$$\tau_d = (d_{LS} + d_{SR})/c \quad (4)$$

TABLE I
PARAMETERS OF THE LED AND THE RGB SENSOR [32], [34]

	Specs	Typical Values	Unit
	Wavelength	635 (Red)	nm
LED	Emitted radiant power (P_e)	0.0033 at $I_F=20$ mA	W
	Viewing angle at half power ($\Phi_{1/2}$)	± 4	deg
	Radiant intensity (I_e)	0.062 ~ 0.180	W/sr
RGB sensor	Irradiance responsivity coefficient (r_e)	2.73 at 645nm 2.04 at 542nm 1.54 at 460nm	V/mW/cm ²
	Detector effective area (A_R)	0.1 × 0.1	cm ²
	Dark voltage (V_D)	15	mV

where c is the speed of light and d_{SR} is the distance between the point S and the sensing face of the RGB sensor. The transfer function of the output voltage of the RGB sensor for the reverse-bias current due to the radiant intensity can also be derived as [30], [31]

$$V_o(s) = \frac{R_r}{R_r C_r s + 1} I_p(s) = \frac{R_r}{\tau_{RC} s + 1} I_p(s) \quad (5)$$

where R_r and C_r are the resistance and capacitance in the RGB amplifier circuit, respectively, τ_{RC} is the time constant of the amplifier circuit, and I_p is the reverse-bias current of the photodiode. From (4) and (5), the bandwidth (BW) of the propagation mechanism can be approximated as (6) in terms of the reciprocal of the total time constant described in Fig. 3(b)

$$f_{BW} \approx \frac{1}{2\pi(\tau_d + \tau_{RC})}. \quad (6)$$

Since the propagation-delay time constant is much smaller than the time constant of the current-to-voltage converter, the BW is mainly governed by the RGB sensor. Eventually, the effective BW of the sensing mechanism is computed at around 4.42 kHz for the maximum-gain condition from the datasheet of the RGB sensor [32]. This effective BW implies that the transfer function of the RGB angle sensor in the control system with a low BW can be expressed by a simple scaling factor and the sensing mechanism can also be modeled from the steady-state characteristics of the RGB sensor. The steady-state output voltage of the RGB sensor can be written as (7) from (5)

$$v_o = R_r i_p. \quad (7)$$

The reverse-bias current of the RGB sensor is expressed linearly in terms of the diode's responsivity (r_ϕ) and the received radiant flux (Φ_e) as [31], [33]

$$i_p = r_\phi \Phi_e. \quad (8)$$

Thus, according to (7) and (8), the output voltage of the RGB sensor for the received irradiance can be derived as

$$v_o = R_r r_\phi \Phi_e = R_r r_\phi A_R E_{rr} = r_e E_{rr} \quad (9)$$

where A_R is the effective sensing area of the RGB sensor, and E_{rr} is the received irradiance. The irradiance responsivity coefficient (r_e) is given in Table I.

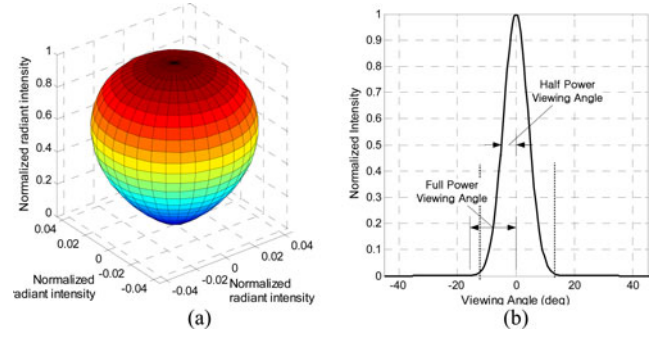


Fig. 4. (a) Normalized 3-D Lambertian radiant intensity pattern of the LED. (b) Normalized radiant intensity according to the angle displacement of the LED (HLMP-EG08-Y2000) used in this paper.

D. Steady-State Propagation Model

The received power of the RGB sensor transmitted from the LED source can be computed effectively by considering the line-of-sight (LOS) propagation path and directed-nonLOS path by using [35]. Since it is assumed that the emission of the LED light source has a Lambertian radiation pattern [30], [35], the radiant intensity according to the viewing angle (θ_v) of the LED is given by

$$I_e(\theta_v) = P_t \left[\frac{m+1}{2\pi} \cos^m(\theta_v) \right] \quad (10)$$

where P_t is the radiant flux (optical power) emitted from the LED, m is the order of the Lambertian emission and given by the semiangle at half power as $m = -\ln 2 / \ln(\cos(\Phi_{1/2}))$ [34], [35], and the half-power angle $\Phi_{1/2}$ is given from the LED datasheet. Fig. 4 shows the normalized three-dimensional (3-D) Lambertian radiant intensity pattern and the definitions for the full power-viewing angle, and a half power-viewing angle of the LED used in this paper.

The irradiance (E_{ts}) and the received optical power (P_{ts}) on the tangential surface on the crossing point S in Fig. 1 can be written as (11) and (12), respectively,

$$E_{ts}(\theta_v) = P_t \left[\frac{m+1}{2\pi} \cos^m(\theta_v) \right] \frac{\cos(\theta_i)}{d_{LS}^2} \quad (11)$$

$$dP_{ts}(\theta_v) = E_{ts}(\theta_v) dA_I \quad (12)$$

where dA_I is the infinitesimal incident-beam area in the vicinity of the point S . The received optical power on the incident surface becomes the new light source of the RGB sensor. The emitted power (P_{rs}) from the surface at point S can be expressed by the linear combination of the Lambertian irradiance and the specular irradiance as [29]

$$dP_{rs}(\theta_v, \theta_r, \varphi_r) = \rho (E_{ts}(\theta_v) + E_{ss}(\theta_i, \theta_r, \varphi_r)) dA_I \quad (13)$$

$$E_{ss}(\theta_i, \theta_r, \varphi_r) = \alpha \exp \left\{ -\frac{1}{2} \left(\left(\frac{\theta_i - \theta_r}{\sigma_s} \right)^2 + \left(\frac{\varphi_r}{2\sigma_s} \right)^2 \right) \right\} \quad (14)$$

where ρ is the reflectance factor that varies according to the reflector type and has the value between 0 and 1, E_{ss} is the irradiance of the specular diffusion function, σ_s is the standard

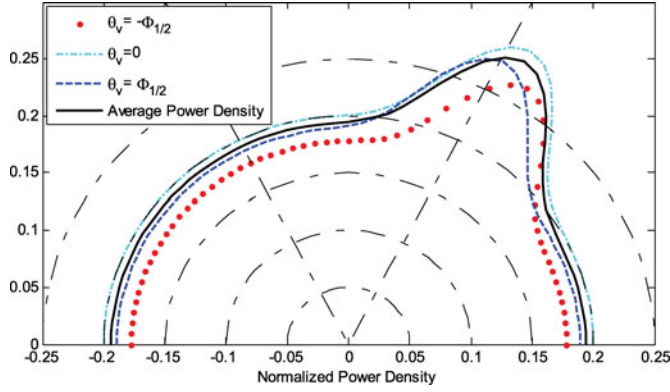


Fig. 5. Expected normalized reflected power density on the tangential surface $(\rho(E_{ts}(\theta_v) + E_{ss}(\theta_i, \theta_r, 0)))/E_{ts}(0)$ with $\rho = 0.2$, $k_s = 0.4$, and $\sigma_s = 10^\circ$.

deviation of roughness of the surface, $\alpha = I_e k_s / (d_{LS}^2 \sqrt{2\pi\sigma_s})$, where k_s that takes the value between 0 and 1 is determined by ρ , and φ_r is the azimuth angle on the surface. The directional diffusion pattern of irradiance in Fig. 5 illustrates that the expected reflected optical power density decreases due to the surface color, surface roughness, and viewing angle of the LED for the single-color surface.

The received irradiance (E_{rr}) on the sensing face of the RGB sensor can be given as

$$dE_{rr}(\theta_v, \theta_r, \phi_r) = \frac{dP_{rs}(\theta_v, \theta_r, \phi_r)}{\pi d_{SR}^2} \cos(\theta_s) \quad (15)$$

where θ_s is the incident angle of the reflected light with respect to the normal vector of the RGB sensing face. The received power is a constant if the stationary system with a constant optical power source has a time-invariant reflectance factor such as a wall or a fixed color surface. However, if the reflectance factor is defined as a function of the rotation angle of the cylindrical color track, the RGB sensor's output voltage can be derived from (9) and (15) as follows:

$$\begin{aligned} v_o(\theta_m, \theta_v, \theta_r, \phi_r) &= r_e E_{rr}(\theta_m, \theta_v, \theta_r, \phi_r) \\ &= r_e P_t \frac{(m+1)}{2\pi^2} \int_{A_I} \Gamma(\theta_m) \frac{\cos^m(\theta_v) \cos(\theta_s)}{d_{LS}^2 d_{SR}^2} (\cos(\theta_i) + B) dA_I \end{aligned} \quad (16)$$

where $B = k_s \exp(-0.5\sigma^2) / \sqrt{2\pi\sigma_s}$, $\sigma = ((\theta_i - \theta_r) / \sigma_s)^2 + (\varphi_r / 2\sigma_s)^2$, and $\Gamma(\theta_m)$ is the reflectance-factor function according to the rotation angle of the cylindrical color track. Additionally, the integration in (16) can be rewritten as a sum (17) with the small cell size and the reflectance factor corresponding to each designated color code in Fig. 2

$$\begin{aligned} v_o(\theta_m, \theta_v, \theta_r, \phi_r) &= r_e P_t \frac{(m+1)}{2\pi^2} \sum_{k=-n}^n \Gamma_k(\theta_m + k\Delta\theta_m) \\ &\quad \times H(k) \Delta A_I \end{aligned} \quad (17)$$

where $2n+1$ is the total number of the RGB cells in the incident area, and $H(k)$ is $[\cos^m(\theta_{vk}) \cos(\theta_{sk}) (\cos(\theta_{ik}) + B_k)] / [d_{LSk}^2 d_{SRk}^2]$. Assuming that the light source with a small viewing angle also has the small incident-beam area due to the

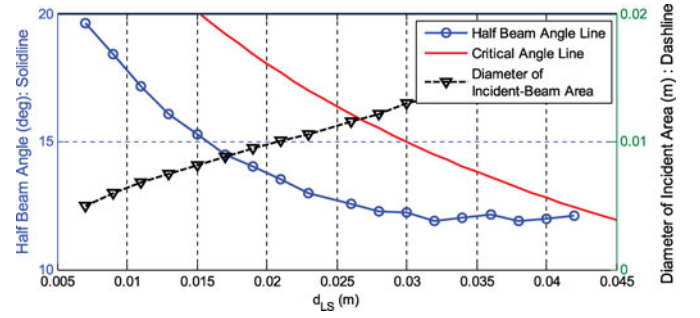


Fig. 6. Diameter of the incident-beam area and the visible viewing angle of the LED according to the displacement of d_{LS} when I_F is 20 mA.

short distance, the irradiance on the incident surface area is the same on the entire incident-beam area. Thus, the output voltage of the RGB sensor can be presented as the product of the constant $H(0)$ and the sum of each reflectance factor of the RGB cells in the incident-beam area corresponding to the rotation angle. This relation can be rewritten by means of the average reflectance factor because the reflectance function is assumed as a function of the rotation angle ($\Gamma_k(\theta_m) = \rho_k \theta_m$)

$$\begin{aligned} v_o(\theta_m) &\approx r_e P_t \frac{(m+1)}{2\pi^2} H(0) [\Gamma_{-n}(\theta_m - n\Delta\theta_m) \\ &\quad + \dots + \Gamma_0(\theta_m) + \dots + \Gamma_n(\theta_m + n\Delta\theta_m)] \Delta A_I \\ &\approx r_e P_t \frac{(m+1)(2n+1)}{2\pi^2} H(0) \Delta A_I \bar{\rho} \theta_m = h_1 \bar{\rho} \theta_m \end{aligned} \quad (18)$$

where $\bar{\rho}$ is the average reflectance factor of the incident area and h_1 is $r_e P_t ((m+1)(2n+1)/2\pi^2) H(0) \Delta A_I$. Since the output voltage in (18) physically implies the sensing angle of the RGB sensor for the mechanical angle, the initial angle-sensing constant of the output voltage for the input angle can be derived as follows:

$$h_1 \bar{\rho} = \frac{v_o(\theta_{m2}) - v_o(\theta_{m1})}{\theta_{m2} - \theta_{m1}} \triangleq K_r \quad (19)$$

where θ_{m1} and θ_{m2} are the minimum and maximum angles of the color track with a full scale range, respectively, $v_o(\theta_{m1})$ and $v_o(\theta_{m2})$ are the output voltages corresponding to each rotation angle, respectively, and K_r is the angle-sensing constant between the RGB sensor and the color track. From (19), the directional angle can be obtained in (20) by defining the RGB code 127 as 0.0°

$$v_o = K_r \theta_m - v_{RGB127}. \quad (20)$$

E. Optimization of Design Parameters

The red LED (HLMP-EG08-Y2000) with a wavelength of 635 nm and a half power at the viewing angle of $\pm 4^\circ$ was used in this paper as shown in Fig. 4(b). The incident-beam area is given by the visible viewing angle that is larger than the half-power viewing angle. The solid and dash lines in Fig. 6 show the visible viewing angle and the diameter of the incident-beam area in accordance with the displacement of d_{LS} defined in Fig. 1, respectively. These measurement results reveal that d_{LS}

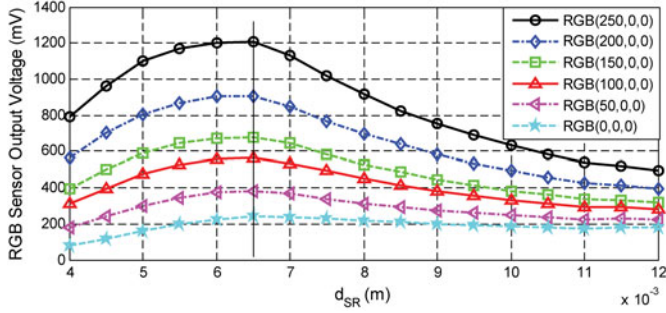


Fig. 7. Output voltages of the-red color channel of the RGB sensor (HDJD-S822-QR999) according to the RGB codes on the cylindrical track and the displacement d_{SR} when $d_{LS} = 0.015$ m, $I_F = 20$ mA, and the physical cell size of each RGB code on the cylinder is 0.0005236×0.01 m².

should be less than 0.042 m due to the critical viewing angle defined in (3) as well as less than 0.017 m due to the maximum allowable incident-beam area. For instance, if the distance is longer than 0.042 m, the larger beam than the critical viewing angle is reflected in the opposite direction. Also, if the distance is longer than 0.017 m, the diameter of the incident area is bigger than the track width of 0.01 m depicted in Fig. 2. Finally, the distance of less than 0.015 m causes the direct interference from the visible viewing angle and blocks the reflected beam path with respect to the configuration of Fig. 1. Hence, the distance was selected as 0.015 m in this paper. The LED's XY-coordinates from the center of the cylinder are as follows:

$$(r_c \sin \theta_C + d_{LS} \sin \theta_L, r_c \cos \theta_C + d_{LS} \cos \theta_L). \quad (21)$$

The experimental data given in Fig. 7 indicate that the optimal displacement of d_{SR} is determined as 0.0065 m in order to obtain the maximum received power and avoid the blocking of the incident beam due to the sensor module, although the output voltages for the linear variation of the RGB codes at the same distance do not have the perfect linear relationship due to the imperfection of the color laser printer (XEROX 7500 Phaser) used in this research.

F. Calibration of the Angle-Sensing Constant

The color laser printer was used to print the color track with only red RGB codes on plain paper. Each cell with its own red RGB code from 0 to 255 (where $G = 0$ and $B = 0$) was sequentially printed with the interval of 1.0° (0.0005236 m) and the track width of 0.01 m as shown in Fig. 2.

Since the undesired ambient light source affects the bias voltage of the RGB sensor, a black plastic cover is used to minimize the magnitude and fluctuation of the bias voltage. Although the measured bias voltage of 36.8 mV (when the LED light source is turned OFF in our indoor lab) was larger than the dark voltage of the RGB sensor of 15 mV, this voltage is still much smaller than the peak voltage for the full RGB code as shown in Fig. 7. Thus, the configuration of Fig. 1 is applicable to angle sensing within the desired angular range.

The color track expressed as the reflectance-factor function in (16) is mainly affected by the printer's color variety as shown

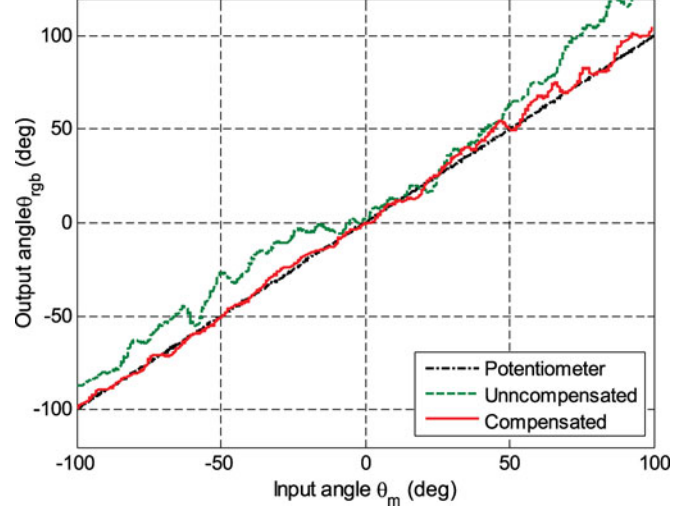


Fig. 8. Uncompensated and compensated angle-sensing outputs (when $I_F = 20$ mA, $\lambda = 635$ nm, $d_{LS} = 0.015$ m, $d_{SR} = 0.0065$ m, $\theta_R = 90^\circ$, $\theta_C = 60^\circ$, $\theta_L = 30^\circ$, and $\theta_v = -15.3^\circ \sim 15.3^\circ$, and the physical cell size of each RGB code on the cylinder is 0.0005236×0.01 m²).

in Fig. 7. The uncompensated result of Fig. 8 shows that the color track using the initially designated sequential red RGB codes from 0 to 255 exhibits the nonlinear characteristics. This implies that the sequential RGB codes should be compensated for to be employed for a new angle-sensing mechanism. For this purpose, the errors of the uncompensated sensing angle were iteratively calibrated with a quarter-error compensation formula (22), and the reference angles were measured by a precision potentiometer (Samuris HP-200) with the nonlinearity of less than 0.1%

$$\theta_{ce} = (\theta_p - \theta_{rgb})/4 \quad (22)$$

where θ_p is the potentiometer angle, θ_{rgb} is the angle of the RGB sensor, and θ_{ce} is the compensated angle. The factor of 4 was empirically selected to make the error converge to zero without error bounce. This is due to the fact that an error is correlated with the other errors in the range of the same incident-beam area. And then, the new RGB code of each angle cell was generated by using (22) and (23)

$$\text{CODE}_{\text{RGB}} = \text{round} [255 (\theta_{rgb} - \theta_{ce})] \quad (23)$$

where CODE_{RGB} is the digital RGB code value from 0 to 255.

The results in Fig. 8 indicate that the nonlinearity for the scaling factor is remarkably improved after four iterations. Eventually, if the bias voltage of (20) is defined as 0° , the transfer function of the RGB angle sensor with a high BW can be expressed as (24) with the angle-sensing constant (K_r^*) compensated for by the quarter-error compensation formula and the least-square estimation

$$v_o \approx K_r^* \theta_m \quad (24)$$

The statistic performance index for the uncompensated and compensated sensing angles in Table II demonstrates that the

TABLE II
STATISTIC PERFORMANCE OF UNCOMPENSATED AND COMPENSATED TRACKS

	Uncompensated	Compensated
Least-square slope (θ_{rgb} / θ_m)	1.05	1.02
Nonlinearity	19.97%	6.63%
Mean error	-13.50°	-1.46°
Standard deviation	9.02°	2.85°

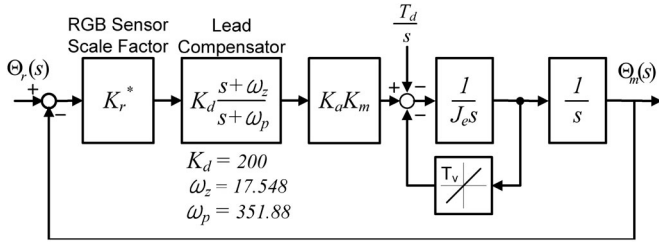


Fig. 9. Closed-loop block diagram of the rotary position-control system.

uncertainties of this RGB angle-sensing mechanism are reduced by the compensation formula given in (22) and (23).

G. Integration Into the Rotary Position-Control System

The closed-loop block diagram in Fig. 9 illustrates the rotary position-control system with a lead compensator and the RGB angle sensor. The phase margin in the position loop with a double integrator is usually insufficient to provide a good response for the abrupt step input command without overshoot in a fast position-control system. To mitigate this drawback, a lead compensator can be a good candidate, leading to a desirable dc gain at low frequency [36]. The closed-loop transfer function for Fig. 9 is described as a continuous form (25) instead of a discrete form because the sampling rate (250 Hz) of the digital controller is much faster than the position loop BW ($\cong 9.6$ Hz)

$$\Theta_m(s) = \frac{K_1(s + \omega_z) \Theta_r(s) + (s + \omega_p) \frac{T_d}{s}}{J_e s^3 + (J_e \omega_p + T_v) s^2 + (T_v \omega_p + K_1) s + K_1 \omega_z} \quad (25)$$

where Θ_m is the mechanical rotation angle, Θ_r is the reference angle, J_e is the effective inertia of the cylinder ($0.00073 \text{ kg}\cdot\text{m}^2$), T_v is the viscous friction ($0.000766 \text{ N}\cdot\text{m}/\text{rad}/\text{s}$), T_d is the Coulomb friction ($0.0062 \text{ N}\cdot\text{m}$) with the sign depending on the rotation direction. K_1 is $K_d K_a K_m K_r^*$, where K_a is the transconductance-amplifier gain ($0.3 \text{ A}/\text{V}$), K_m is the torque constant of the motor ($0.3875 \text{ N}\cdot\text{m}/\text{A}$), and K_r^* is the scale factor of the RGB sensing angle ($0.425 \text{ V}/\text{rad}$).

The simulation results in Fig. 10 show the frequency responses of the uncompensated and compensated rotary position-control systems. The uncompensated system has the phase margin of 26° at the gain crossover frequency of 1.3 Hz. On the other hand, the compensated system has the improved phase margin of 52° at the gain crossover frequency of 7.0 Hz as well as the ten times increased low frequency gain by the applied lead compensator.

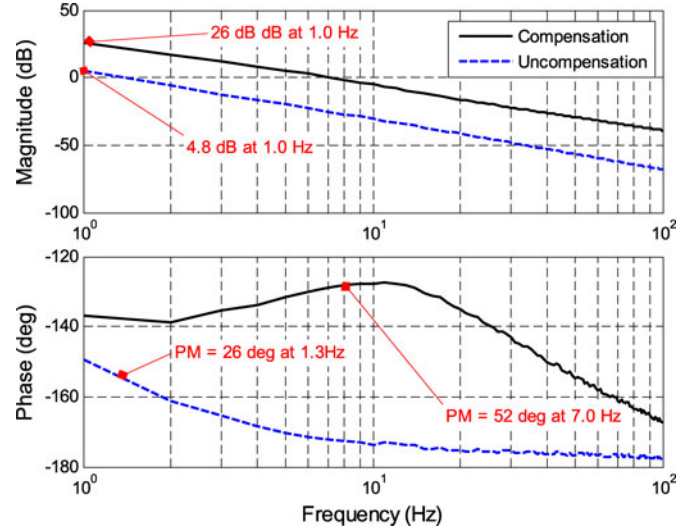


Fig. 10. Frequency responses of the uncompensated and compensated rotary position-control systems.

III. HARDWARE IMPLEMENTATION

The hardware block diagram in Fig. 11 shows the test bed of the rotary position-control system implemented with six components: the mechanical part consisting of a cylindrical inertia, brush-type DC motor, mechanical coupler, and rotary potentiometer; the color sensor module; the sensor interface board between the color sensor and a digital signal processor (DSP) module; the TMS320F28069 module (control stick by Texas Instruments) running the digital controller and the real-time serial communication with a LabView console on a PC; a DAQ (data acquisition, ACPI-3120 by ADDI-DATA) board generating the analog voltage output corresponding to the control command received from the DSP; the analog-output circuit board interfacing between the DAQ board and the transconductance amplifier. The DSP with a 1-kHz update rate generates the control command using the error between the reference command and the filtered output voltage of the RGB sensor through an internal 12-bit ADC built in the DSP.

The lead compensator implemented on the DSP outputs the control command into the DAQ board through the RS422 serial communication at 250 Hz. This command is conveyed through the DAC of the DAQ board by LabView. The output voltage of the DAC is delivered as a current output through the transconductance amplifier. The motor starts to rotate to reach the desired reference angle. The color-sensing module measures the irradiance change of the reflected light corresponding to the rotation angle, and then, converts it into the voltage output proportional to the reflected luminous intensity.

IV. EXPERIMENTAL RESULTS

In this section, key experimental results are presented and discussed to demonstrate the performance of the new high-resolution angle-sensing mechanism employed in the rotary position-control test bed shown in Fig. 12.

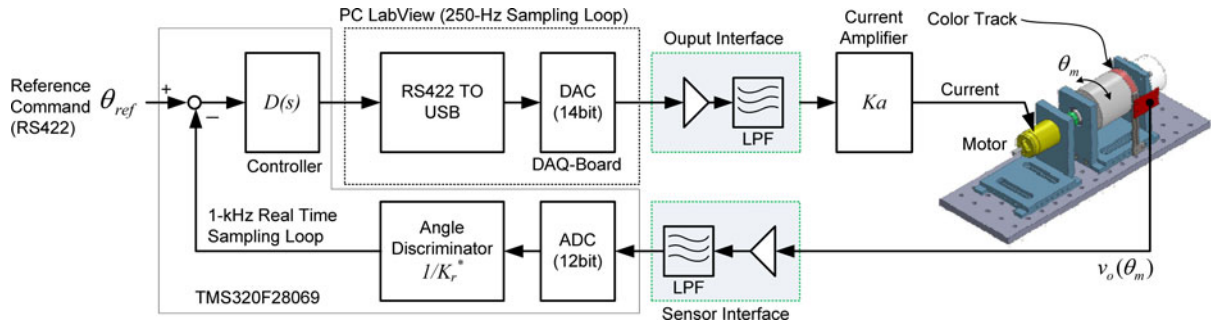


Fig. 11. Hardware block diagram of the rotary position-control system.

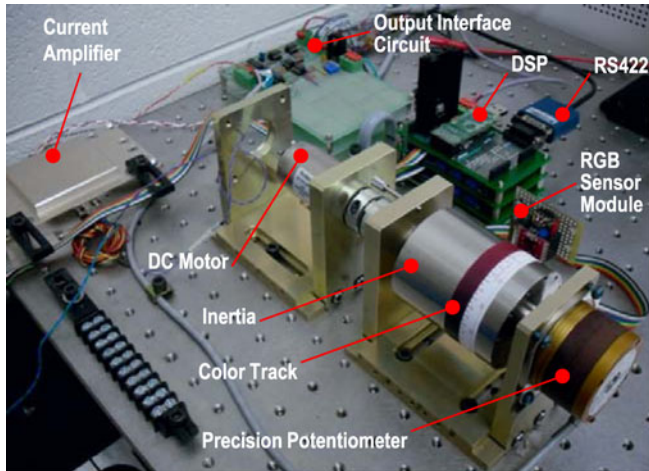


Fig. 12. Rotary position-control system (with the uncovered RGB sensor).

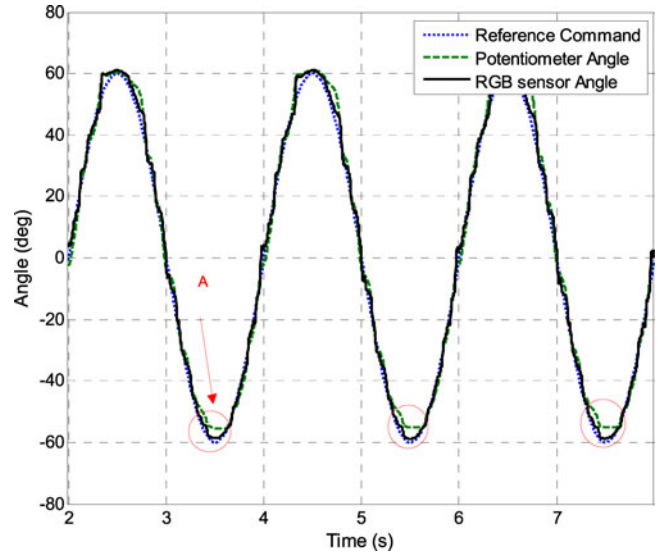


Fig. 14. Response to a sinusoidal reference input with the magnitude of 60° and the period of 2 s.

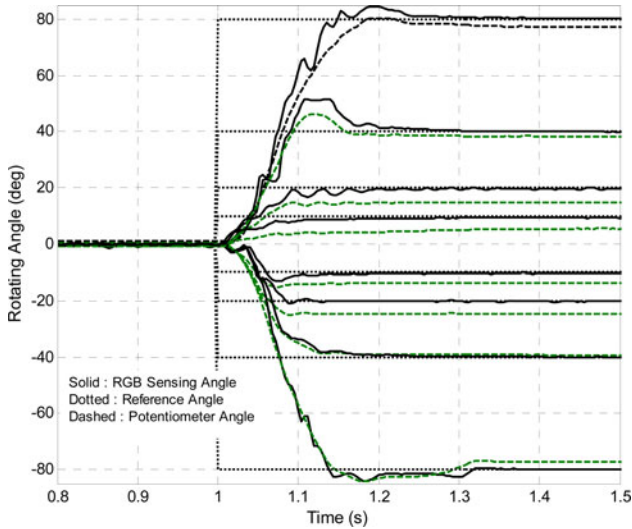


Fig. 13. Step responses to various reference angle commands ($\pm 10^\circ$, $\pm 20^\circ$, $\pm 40^\circ$, and $\pm 80^\circ$).

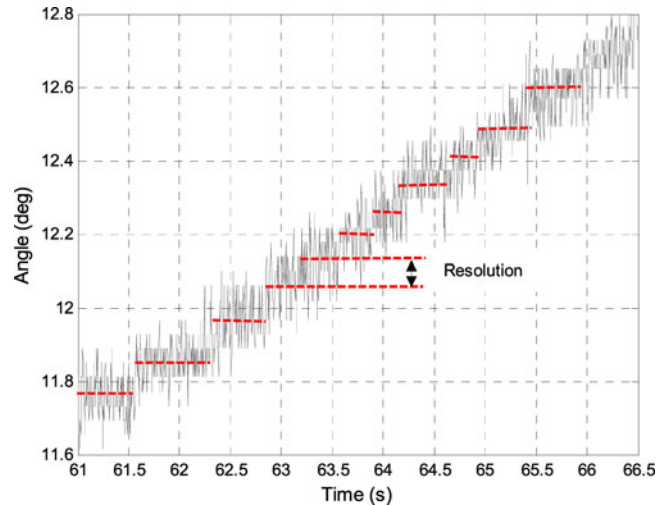


Fig. 15. Resolution of the rotary position-control system with the new sensing mechanism.

The step responses in Fig. 13 follow the reference angle commands very closely even if there are some jerks or ridges during the transient interval due to the nonlinearity of the RGB sensing angle. In addition, the maximum steady-state errors are less than 0.4° .

The response to a sinusoidal reference command with the magnitude of 60° shown in Fig. 14 tracks the input command well. The repeated differences between the potentiometer angle and the RGB sensing angle shown in the mark "A" of

Fig. 14 originated from the nonlinearity discussed in Section II-F. Although these nonlinear behaviors hinder more accurate responses, this cost-effective sensing mechanism is sufficient to be used in a fast position-control system with permissible error bounds. Thus, both step- and sinusoidal-response results proved the feasibility that this new angle-sensing mechanism can be employed in a precision rotary position-control system.

The repetitive step responses in Fig. 15 show the resolution of the sensing angle. The resolution, which is the angular interval divided by the total number of step change, is found to be around 0.08° . This value is essentially the same as the resolution of the ADC implemented in this system.

V. CONCLUSION

The main purpose of this research is to develop a new cost-effective angle-sensing mechanism that can be employed in a high-resolution rotary position-control system with fast dynamics. For this purpose, a noncontact RGB sensor was used. A comprehensive model for this sensing mechanism was derived on the basis of the directed non-LOS path, directional diffusion model, and Lambertian emission pattern of the LED light source. The color track with the reflectance factor corresponding to the rotation angle was printed on plain paper by a commercial color printer. The reflectance factor for each small cell of the color track was controlled by compensating for the designated RGB codes. The feasibility of this sensing system was demonstrated with the promising results such as the high BW of 4.42 kHz, the mean error of -1.46° , the standard deviation of 2.85° , and the high resolution of 0.08° limited by the ADC's resolution. These results can be much improved with accurate color-printing techniques and paper-quality controls. In the end, the performance of the rotary position-control system using this sensing mechanism was successfully demonstrated with various step and sinusoidal responses. These experimental results are well in agreement with our analysis and simulation.

REFERENCES

- [1] K. Ohnishi, M. Shibata, and T. Murakami, "Motion control for advanced mechatronics," *IEEE/ASME Trans. Mechatronics*, vol. 1, no. 1, pp. 56–67, Mar. 1996.
- [2] B. S. Methven, "The design, construction and performance of thick film cermet trimming potentiometers," *Radio Electron. Eng.*, vol. 37, no. 1, pp. 17–21, Jan. 1969.
- [3] A. Green and K. Schulz, "Environmental effects on precision potentiometers," *IRE Trans. Compon. Parts*, vol. 4, no. 1, pp. 18–23, Mar. 1957.
- [4] D. G. Alciatore and M. B. Histand, *Introduction to Mechatronics and Measurement Systems*, 4th ed. New York, NY, USA: McGraw-Hill, 2012, pp. 383–389.
- [5] C. Attaianesi, G. Tomasso, and D. DeBonis, "A low cost resolver-to-digital converter," in *Proc. IEEE Int. Electr. Mach. Drives Conf.*, 2001, pp. 917–921.
- [6] L. Ben-Brahim, M. Benammar, M. A. Alhamadi, and M. A. Al-Hitmi, "A new low cost linear resolver converter," *IEEE Sensors J.*, vol. 8, no. 10, pp. 1620–1627, Oct. 2008.
- [7] C. Attaianesi and G. Tomasso, "Position measurement in industrial drives by means of low-cost resolver-to-digital converter," *IEEE Trans. Instrum. Meas.*, vol. 56, no. 6, pp. 2155–2159, Dec. 2007.
- [8] M. Dimmler and C. Dayer, "Optical encoders for small drives," *IEEE/ASME Trans. Mechatronics*, vol. 1, no. 3, pp. 278–283, Mar. 1996.
- [9] R. S. Popovic, C. Schott, P. M. Drljaca, and R. Racz, "A new CMOS Hall angular position sensor," *Tech. Messen.*, vol. 68, no. 6, pp. 286–291, Jun. 2001.
- [10] C. Schott, R. Racz, and S. Huber, "Novel analog magnetic angle sensor with linear output," *Sens. Actuators A, Phys.*, vol. 132, no. 1, pp. 165–170, Nov. 2006.
- [11] S. Foong, K. M. Lee, and K. Bai, "Harnessing embedded magnetic field for angular sensing with nanodegree accuracy," *IEEE/ASME Trans. Mechatronics*, vol. 17, no. 4, pp. 687–696, Aug. 2012.
- [12] Y. Y. Lee, R. H. Wu, and S. T. Xu, "Applications of linear Hall-effect sensors on angular measurement," in *Proc. IEEE Int. Conf. Control Appl.*, Sep. 2011, pp. 479–482.
- [13] P. Fulmek, F. Wandling, W. Zdiarsky, G. Brasseur, and S. Cermak, "Capacitive sensor for relative angle measurement," *IEEE Trans. Instrum. Meas.*, vol. 51, no. 6, pp. 1145–1149, Dec. 2002.
- [14] M. H. Cheng, G. T. C. Chiu, and M. A. Franchek, "Real-time measurement of eccentric motion with low-cost capacitive sensor," *IEEE/ASME Trans. Mechatronics*, vol. 18, no. 3, pp. 990–997, Jun. 2013.
- [15] F. Kimura, M. Gondo, A. Yamamoto, and T. Higuchi, "Resolver compatible capacitive rotary position sensor," in *Proc. IEEE Int. Ind. Electron.*, Nov. 2009, pp. 1923–1928.
- [16] A. Cavallo, G. De Maria, C. Natale, and S. Pirozzi, "Optoelectronic joint angular sensor for robotic fingers," *Sens. Actuators A, Phys.*, vol. 107, no. 1, pp. 21–25, Oct. 2003.
- [17] T. W. Ng, "The optical mouse as a two-dimensional displacement sensor," *Sens. Actuators A, Phys.*, vol. 152, no. 2, pp. 203–210, Jun. 2009.
- [18] K. M. Lee and D. Zhou, "A real-time optical sensor for simultaneous measurement of three-DOF motions," *IEEE/ASME Trans. Mechatronics*, vol. 9, no. 3, pp. 499–507, Sep. 2004.
- [19] M. Umberto and A. Signorini, "Low-cost optical motion sensors: An experimental characterization," *Sens. Actuators A, Phys.*, vol. 128, no. 2, pp. 402–408, Apr. 2006.
- [20] M. Tresanchez, T. Pallejà, M. Teixidó, and J. Palacín, "The optical mouse sensor as an incremental rotary encoder," *Sens. Actuators A, Phys.*, vol. 155, no. 1, pp. 73–81, Oct. 2009.
- [21] M. Tresanchez, T. Pallejà, M. Teixidó, and J. Palacín, "Using the image acquisition capabilities of the optical mouse sensor to build an absolute rotary encoder," *Sens. Actuators A, Phys.*, vol. 157, no. 1, pp. 161–167, Jan. 2010.
- [22] T. Gevers and A. W. M. Smeulders, "Color-based object recognition," *Pattern Recognit.*, vol. 32, no. 3, pp. 453–464, Feb. 1999.
- [23] A. Sivanantha Raja and K. Sankaranarayanan, "Performance analysis of a colorimeter designed with RGB color sensor," in *Proc. IEEE Int. Intell. Adv. Syst. Conf.*, Nov. 2007, pp. 305–310.
- [24] M. Nkomo and M. Collier, "A color-sorting SCARA robotic arm," in *Proc. IEEE 2nd Int. Consum. Electron., Commun. Netw. Conf.*, Nov. 2012, pp. 763–768.
- [25] M. Seelye, G. S. Gupta, D. Bailey, and J. Seelye, "Low cost colour sensors for monitoring plant growth in a laboratory," in *Proc. IEEE Int. Instrum. Meas. Technol. Conf.*, May 2011, pp. 1–6.
- [26] H. S. Cho, *Optomechanics Fusion of Optical and Mechatronic Engineering*, 1st ed. Boca Raton, FL, USA: CRC Press, 2006, ch. 2.
- [27] X. D. He, K. E. Torrance, F. X. Silicon, and D. P. Greenberg, "A comprehensive physical model for light reflection," *Comput. Graph.*, vol. 25, no. 4, pp. 175–186, Jul. 1991.
- [28] H. Li and K. E. Torrance, "A practical, comprehensive light reflection model," Program of Computer Graphics, Tech. Rep. PCG-05-03, Cornell Univ., Ithaca, NY, 2005.
- [29] S. K. Nayar, K. Ikeuchi, and T. Kanade, "Surface reflection: physical and geometrical perspective," *IEEE Trans. Pattern Anal. Mach. Intell.*, vol. 13, no. 7, pp. 611–633, Jul. 1991.
- [30] E. F. Schubert, *Light-Emitting Diodes*, 2nd ed. Cambridge, U.K.: Cambridge Univ. Press, 2006, chs. 4, 16, 24.
- [31] J. Graeme, *Photodiode Amplifiers OP Amp Solution*. New York, NY, USA: McGraw-Hill, 1995, ch. 1.
- [32] AVAGO Technologies, HDJD-S822-QR999 RGB Color Sensor Data Sheet. (Feb. 2007). [Online]. Available: www.avagotech.com
- [33] AVAGO Technologies, "Reflective color sensing with RGB color sensor," White Paper AV02-0172EN, Mar. 2010.
- [34] AVAGO Technologies, HLMP-EG08-Y2000 AllnGap LED Lamps Data Sheet. (Sep. 2008). [Online]. Available: www.avagotech.com
- [35] T. Komine and M. Nakagawa, "Fundamental analysis for visible-light communication system using LED light," *IEEE Trans. Consum. Electron.*, vol. 50, no. 1, pp. 100–107, Feb. 2004.
- [36] G. F. Franklin, J. D. Powell, and A. Emami-Naeini, *Feedback Control of Dynamic System*, 6th ed. Englewood Cliffs, NJ, USA: Prentice-Hall, 2010.



Young-shin Kwon (S'11) received the B.S. and M.S. degrees in control and instrumentation engineering from Hanyang University and Seoul National University, Seoul, Korea, in 1995 and 1997, respectively. He is currently working toward the Ph.D. degree in the Department of Mechanical Engineering, Texas A&M University, College Station, TX, USA.

Following receipt of the M.S. degree, he was with Hyundai Electronics Corporation, Icheon, Korea, for two years. He also worked as a Principle Researcher with LIG Nex1 Corporation, Yong-In, Korea, for 13 years. His research interests include design and analysis of spatial stabilization of multiaxis platforms, optomechatronics systems, and linear magnetic actuators.



Won-jong Kim (S'89–M'97–SM'03) received the B.S. (*summa cum laude*) and M.S. degrees in control and instrumentation engineering from Seoul National University, Seoul, Korea, in 1989 and 1991, respectively, and the Ph.D. degree in electrical engineering and computer science from the Massachusetts Institute of Technology, Cambridge, MA, USA, in 1997.

Since 2000, he has been with the Department of Mechanical Engineering, Texas A&M University (TAMU), College Station, TX, USA, where he is currently an Associate Professor and was the inaugural holder of the Dietz Career Development Professorship II in 2007–2010. His current research interests include the analysis, design, and real-time control of mechatronic systems, networked control systems, and nanoscale engineering and technology. He is the holder of three U.S. patents on precision positioning systems.

Dr. Kim is a Fellow of the American Society of Mechanical Engineers (ASME) and a member of Pi Tau Sigma. He is or was a Technical Editor for the *IEEE/ASME TRANSACTIONS ON MECHATRONICS*, *ASME Journal of Dynamic Systems, Measurement and Control*, *International Journal of Control, Automation, and Systems*, and *Asian Journal of Control*.